Concept for Pulse Compression Device Using Structured Spatial Energy Distribution

Venkata Ananth Tamma, Alexander Figotin, and Filippo Capolino, *Senior Member, IEEE*

Abstract—We explore a novel concept for pulse compression scheme applicable at RF, microwave, and possibly up to optical frequencies based on structured energy distribution in cavities supporting degenerate band-edge (DBE) modes. We show the high spatial concentration of energy due to DBE modes and proper choice of boundary conditions in coupled transmission lines (TLs) provide the basis for superior performance of the structured cavity when compared to a conventional cavity. We investigate the novel cavity features: larger loaded quality factor of the cavity and stored energy compared to conventional designs, robustness to variations of cavity loading, energy feeding and extraction at the cavity center, and substantial reduction of the cavity size by use of equivalent lumped circuits for low-energy sections of the cavity. Structured energy also allows for controlled pulse shaping via engineered extraction techniques. The presented concepts are general, in terms of equivalent coupled TLs, and can be applied to a variety of realistic guiding structures. Potential applications include microwave pulse compression devices, on-chip millimeter-wave pulse generation, and pulsed laser generation.

Index Terms—Cavity resonators, high-power microwave generation, optical pulse compression, photonic-bandgap structures, pulse compression methods, Q-factor.
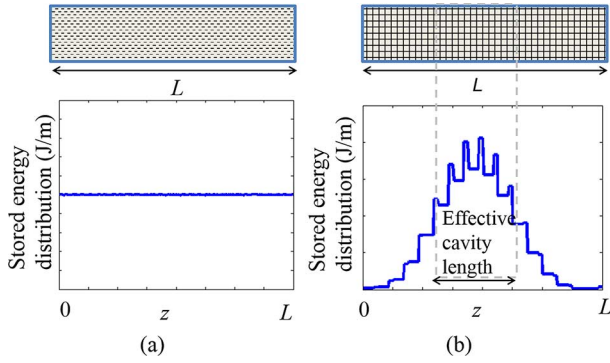
Fig. 1. Plots of spatial distribution of total time-average energy units of (J/m) versus position z in: (a) conventional $n(\lambda/2)$ cavity of length L and (b) structured cavity of same length L. In (b), about 60% of the total stored energy is stored in just 25% of the total cavity length. (a) Conventional $n(\lambda/2)$ cavity. (b) Structured cavity (DBE modes).

allowing for extraction of maximum amount of energy in the minimal possible time. An example of such a structured energy distribution, shown schematically in Fig. 1(b), plots the spatial distribution of the sum of stored time average electric and magnetic energy density (units of J/m) for a novel structured cavity having the same length L as the conventional $n(\lambda/2)$ cavity resonator. In contrast to the constant energy distribution in the conventional cavity shown in Fig. 1(a), we find that most of the energy in Fig. 1(b) is stored with a small region around the cavity center. This allows releasing the stored energy faster due to the reduction of the effective cavity length and this concept is the basis for the work presented in this paper.

Such concentrated energy distribution is also helpful to control losses in structured cavity thereby improving the cavity Q. It is well known that the skin-effect loss is frequency dependent (see [16, Ch. 1] and [17, Ch. 2]) and at lower frequencies, typically below 1 GHz, the skin-effect loss could be neglected (see [16, Ch. 1] and [17, Ch. 2]). It is possible to use cavities whose walls are coated with a thin layer of low-loss metals like gold or silver to reduce skin-effect losses. Since the energy in a conventional $n(\lambda/2)$ cavity resonator is uniformly distributed, to control losses the entire cavity has to be coated with gold or silver. However, a structured energy distribution allows for engineering the losses in only a small region of the cavity thereby further increasing the cavity Q due to further reduction in losses using better materials only in those unit cells where most of the energy is stored.

We propose in this paper a concept for a novel structured cavity (i.e., with structured energy distribution) with applications to MPC devices. The cavity is composed of a cascade of N unit cells, properly designed, each supporting two distinct electromagnetic modes (four, if distinguishing between forward and backward modes), thereby leading to distributed storage of energy in the cavity. The cavity Q is very large and importantly it is *insensitive to loading* by source impedances. Such a cavity presents a novel feature compared to a standard cavity whose Q is dramatically reduced when loaded by source impedance. The structured energy distribution also helps in efficient feeding and evacuation of accumulated energy from the center of the cavity. It also permits for substantial reduction in cavity size by

allowing for lumped circuit implementation of those unit cells with lower stored energy. Another unique feature of the structured cavity is the preservation of spatial energy distribution around the cavity center with increasing number of unit cells N.

The novel features of the structured cavity are partly due to degenerate band-edge (DBE) modes [18]–[20]. DBE modes are unique band-edge phenomenon supported by periodic structures. At the DBE frequency, the photonic dispersion curve $\omega(k)$ follows a degenerate fourth power dependence of the radian frequency ω on the Bloch wave vector k, instead of second power dependence associated with typical band-edge resonances [18]–[20]. This leads, in particular, to vanishing of the group velocity and consequent dramatic increase in the field intensity inside a finite stack exhibiting the DBE mode [18]–[20]. The concept of DBE [18]–[20] was first proposed in a simple structure composed of stacked anisotropic dielectric layers [18]–[20], where the importance of symmetry breaking in achieving the DBE was emphasized. Planar circuits supporting DBE modes were developed in analogy to propagation of light in the stacked anisotropic dielectric layers [22], [23]. Recently it has been shown that the DBE can be obtained in all-metallic circular waveguides with periodic loading [24]. The proposed pulse compression concepts can be applied to all structures summarized in Appendix A. Previously, it has been shown that field intensity enhancement varied as the fourth power of the number of unit cells N within the stack [18]–[20] and was found to be true only for large N [23]. The finite stack supporting DBE modes is ideally suited for highly frequency selective applications such as resonant cavities due to the narrow line shapes associated with the transmission band-edge resonance as evident from [18]–[20]. Although the enhancement of field intensity in finite stacks have been discussed [18]–[20], the application of DBE modes to cavities with known boundary termination and feeding method has not been explored.

In this paper, we study novel periodic structured cavities, which not only make use of the energy concentration due to DBE modes, but also use proper choice of boundary and feeding conditions to achieve superior loaded Q factor compared to standard cavities. While various different cavity configurations are conceivable, in this paper we study a particular cavity configuration in which we feed and extract energy from the cavity center. The basic configuration of the structure consists of a finite periodic stack of unit cells, as was done in [18]–[20], but terminated here in short circuits with energy feeding and extraction from the center of the cavity. In line with the definition of active MPC devices [1]–[3], [9] we show that the Q of this novel structured cavity can be dramatically altered by simple modifications to the structure, thereby enhancing its appeal for use in MPC applications. This paper is organized as follows. In Section II, we describe the unit cell design, which is made up of periodic coupled TLs made of two cascading TLs, with periodic coupling. It is understood that the equivalent TL model can be an exact field representation of complex realistic waveguiding systems [25]–[27]. Therefore, a periodic multi transmission line (MTL) is representative of a periodic cascade of multimode waveguide sections shown in Appendix A. To develop

a DBE, two coupled modes in each direction are necessary, and a variety of structures may support such conditions, including closed metallic waveguides for high-power applications. In this work, structured cavities based on the DBE condition are modeled using cascaded sections of MTLs. In Section III, we describe the structured cavity made up of a finite number of unit cells N and discuss key attributes of the cavity such as quality factor and density of stored energy. In Section IV, we present an illustrative implementation of the unit cell of Section II and describe two states of the structure with dramatic differences in the quality factors. In addition, we discuss applications of the structured cavity to MPC devices. Although the concept of structured cavity is being introduced with MPC applications, we expect that it can be applied to printed or integrated RF circuits and optical devices.

II. UNIT CELL DESIGN AND FORMALISM

The design of the unit cell is fundamental to the operation of the structured cavity. A unit cell can be formed by a few possible constituents and by several TLs, though in the remainder of this paper we focus on having only two TLs. The unit cell consisting of three MTL sections, for example, shown schematically in Fig. 12(d) and [24], was designed in analogy to the anisotropic dielectric layer unit cell in [18]–[20]. The unit cell consisting of two MTL sections was designed starting from the unit cell with three MTL sections and then compacting the equations. A similar design was used in [22] and [23]. For example, the unit cell of the waveguide structure in Fig. 12(d) is made up of three MTL segments. This suggests a high degree of flexibility in the implementation of unit cells supporting DBE modes. The unit cells in the paper consist of two MTL segments A, B of lengths d_A and d_B shown schematically in Fig. 2(a). Each MTL segment here consists of *two* TLs. These are chosen here to be uncoupled in segment A and coupled by distributed coupling capacitance in segment B, though many other configurations are possible and would lead to analogous results. A few possible implementation configurations of the unit cell supporting the DBE condition are detailed in Appendix A. The theoretical formulation for MTLs is well known and we follow the notation presented in [28]–[30]. We denote

$$\underline{\mathbf{Z}}_A = \underline{\mathbf{R}}_{s,A} + j\omega\underline{\mathbf{L}}_A \quad \underline{\mathbf{Y}}_A = j\omega\underline{\mathbf{C}}_A \qquad (1)$$

and

$$\underline{\mathbf{Z}}_B = \underline{\mathbf{R}}_{s,B} + j\omega\underline{\mathbf{L}}_B \quad \underline{\mathbf{Y}}_B = j\omega\underline{\mathbf{C}}_B \qquad (2)$$

to be the series impedance and shunt admittance matrices, per unit length, of segments A and B. Here, we define

$$\underline{\mathbf{R}}_{s,A} = \begin{bmatrix} R_{s,A1} & 0 \\ 0 & R_{s,A2} \end{bmatrix} \quad \underline{\mathbf{R}}_{s,B} = \begin{bmatrix} R_{s,B1} & 0 \\ 0 & R_{s,B2} \end{bmatrix} \qquad (3)$$

as the resistance matrices (with per unit length entries) for the segments A and B, respectively. We also define

$$\underline{\mathbf{L}}_A = \begin{bmatrix} L_{A,11} & 0 \\ 0 & L_{A,22} \end{bmatrix} \quad \underline{\mathbf{L}}_B = \begin{bmatrix} L_{B,11} & 0 \\ 0 & L_{B,22} \end{bmatrix} \qquad (4)$$
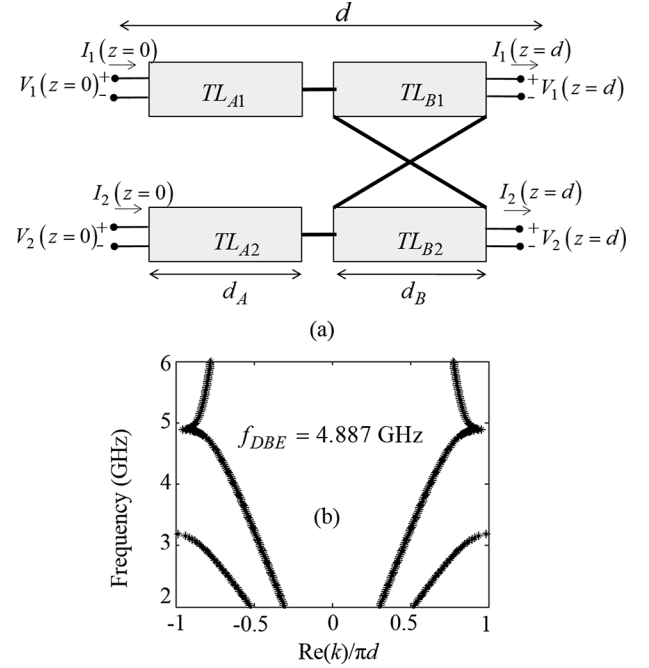

Fig. 2. (a) Schematic of a unit cell with two coupled TLs capable of supporting a DBE mode. (b) Plot of the Re(k)-ω dispersion diagram for a periodic MTL cascading unit cells using the parameter values detailed in Appendix B. (a) Schematic of unit cell.

as the inductance matrices (with per unit length entries) for segments A and B, respectively, and

$$\underline{\mathbf{C}}_A = \begin{bmatrix} C_{A,11} & 0 \\ 0 & C_{A,22} \end{bmatrix}$$

$$\underline{\mathbf{C}}_B = \begin{bmatrix} C_{B,11} + C_{B,12} & -C_{B,12} \\ -C_{B,12} & C_{B,22} + C_{B,12} \end{bmatrix} \qquad (5)$$

as the capacitance matrices (with per unit length entries) for the segments A and B, respectively, where, $(L_{i,nn}, C_{i,nn})$ are the line inductance and capacitance, respectively, of the nth TL ($n = 1, 2$) in the ith ($i = A, B$) segment, $C_{B,12} = C_{B,21}$ is the distributed coupling capacitance in segment B and ω is the radian frequency of operation. Here, we choose the two TLs in section A, TL_{A1} and TL_{A2}, to be dissimilar and the two TLs in section B, TL_{B1} and TL_{B2}, to be identical. Absence or presence of coupling breaks the symmetry between segments A and B. All TLs in sections A and B are assumed to have some losses represented by line resistances series, which model the ohmic loss on the surface of metals in real waveguides. We also assume lossless coupling between the two guided fields, represented by the two coupled TLs.

It is convenient to define the state-vector of the form $\boldsymbol{\psi}(z) = \begin{bmatrix} V_1 & V_2 & I_1 & I_2 \end{bmatrix}^T$, where $V_1(z)$, $I_1(z)$ and $V_2(z)$, $I_2(z)$ are the voltages and currents at a point z on the upper and lower sets of TLs in the cavity. The first-order differential equations for the MTL in terms of the impedance and admittance matrix is written as

$$\frac{\partial}{\partial z}\boldsymbol{\psi}(z) = -\underline{\mathbf{M}}\boldsymbol{\psi}(z) \qquad (6)$$

where

$$\underline{\mathbf{M}} = \begin{bmatrix} \mathbf{0} & \mathbf{Z} \\ \mathbf{Y} & \mathbf{0} \end{bmatrix} \tag{7}$$

where $\underline{\mathbf{Z}}$ and $\underline{\mathbf{Y}}$ are the impedance and admittance matrices describing the per unit parameters of the MTL. Denoting $\boldsymbol{\psi}(z_0) = \boldsymbol{\psi}_0$ as the initial TL values at z_0, assuming that $\underline{\mathbf{M}}$ does not change with z (i.e., for a uniform TL), we recognize (6) as the well-known Cauchy problem [18]–[20] with a unique solution $\boldsymbol{\psi}(z) = \underline{\mathbf{T}}(z, z_0)\boldsymbol{\psi}(z_0)$, where we define the matrix $\underline{\mathbf{T}}(z, z_0)$, which uniquely relates the state vector $\boldsymbol{\psi}(z)$ between two known points z_0 and z as $\underline{\mathbf{T}}(z, z_0) = e^{-\underline{\mathbf{M}}(z - z_0)}$.

Extending this concept to cascaded segments of MTL structures as in Fig. 2(a), in the remainder of this paper it is convenient to resort to the definition of the $ABCD$ transfer matrix (see [16, Ch. 4] and [17]), commonly used in microwave engineering, and used here as generalized to multiple ports [28], [31]. We define the $ABCD$ matrix for each section, A and B, of the four-port circuits in Fig. 2(a) as $\underline{\mathbf{T}}_A \equiv \underline{\mathbf{T}}(z_0 - d_A, z_0) = e^{\underline{\mathbf{M}}d_A}$ and $\underline{\mathbf{T}}_B \equiv \underline{\mathbf{T}}(z_0 - d_B, z_0) = e^{\underline{\mathbf{M}}d_B}$, where

$$\underline{\mathbf{M}}_A = \begin{bmatrix} \mathbf{0} & \mathbf{Z}_A \\ \mathbf{Y}_A & \mathbf{0} \end{bmatrix} \quad \underline{\mathbf{M}}_B = \begin{bmatrix} \mathbf{0} & \mathbf{Z}_B \\ \mathbf{Y}_B & \mathbf{0} \end{bmatrix} \tag{8}$$

and $\underline{\mathbf{0}}$ is a zero matrix of order 2. It is customary to implicitly assume $z < z_0$ in microwave engineering (see [16, Ch. 4] and [17]), and therefore the argument is dropped in the remainder of this paper. We can express the 4×4 $ABCD$-like transfer matrix $\underline{\mathbf{T}}_U$ of the unit cell shown in Fig. 2(a), as the product of two 4 $\times$ 4 matrices describing the transfer matrices of the individual sections of the unit cell

$$\underline{\mathbf{T}}_U = \underline{\mathbf{T}}_A \underline{\mathbf{T}}_B. \tag{9}$$

For an infinitely long stack of TL unit cells, a periodic solution for the state vector $\boldsymbol{\psi}(z)$ exists in the Bloch form

$$\boldsymbol{\psi}(z + d) = e^{-jkd}\boldsymbol{\psi}(z) \tag{10}$$

where k is the Bloch wavenumber, which assumes complex values when losses are present and when describing the bandgap. To determine the Bloch wavenumber, we can write the following eigenvalue equation:

$$\underline{\mathbf{T}}_U \boldsymbol{\psi}(0) = e^{jkd}\boldsymbol{\psi}(0) \tag{11}$$

such that the four eigenvalues $\lambda_i = e^{jk_i d}$, $i = 1, 2, 3, 4$, of the $\underline{\mathbf{T}}_U$ operator are obtained as solutions of the characteristic equation

$$\mathrm{Det}\left(\underline{\mathbf{T}}_U - \lambda \underline{\mathbf{1}}\right) = 0 \tag{12}$$

where we define $\underline{\mathbf{1}}$ to be the identity matrix of order 4. The $\mathrm{Re}(k)$-ω dispersion diagram, of the unit cell structure of Fig. 2(a) is plotted in Fig. 2(b) for the TL values given below. The structure exhibits the DBE mode at 4.887 GHz at the edge of the Brillouin zone. In this paper, a constant distributed loss series line resistance $R_s = 1$ (mΩ/m), in the order of magnitude of the metal surface resistivity of copper in the
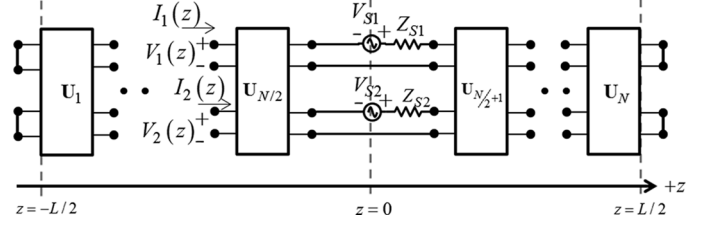

Fig. 3. Schematic of structured cavity formed by cascading N unit cells of two coupled TLs.

hundreds of the MHz to GHz regime, is used in all numerical calculations. The distributed shunt conductance is always set to zero. All results are obtained for the structured cavity fed by one ideal voltage source $V_{S1} = 1$ (V) and $V_{S2} = 0$. All unit cells in this work have a nominal length $d = 1$ (cm). We note at the DBE resonance frequency of 4.887 GHz, the free-space wavelength $\lambda_0 \approx 6.14$ (cm). The following are the parameters of the MTLs for the unit cell in Fig. 2(a): (segments A and B are mentioned in subscripts) $d_A = 0.265$ (cm), $d_B = 0.735$ (cm), $L_{A,11} = L_{A,22} = 0.2$ (μH/m), $L_{B,11} = L_{B,22} = 0.2$ (μH/m), $C_{A,11} = 2$ (nF/m), $C_{A,22} = 0.2$ (nF/m), $C_{B,11} = C_{B,22} = 0.2$ (nF/m), and $C_{B,12} = C_{B,21} = 150$ (pF/m). We find that the above parameter values are of the same order of magnitude as the equivalent MTL parameters for the structures in Fig. 12(d) and [24]. This suggests that structured cavities supporting DBE modes can be implemented using practical waveguiding structures. These values are also repeated in Appendix B for convenience.

For the losses considered, the plot in Fig. 2(b) is similar to the one for the case without losses since small losses do not significantly perturb the DBE condition. Note that in each TL segment we assume there is only one modal wavenumber (for both modes in opposite directions). Therefore the periodic MTL supports four Bloch modes (with $\pm k$ symmetry due to reciprocity), the solution of (11). The degeneracy condition associated to the DBE is among these four Bloch modes. The $ABCD$-like transfer matrix $\underline{\mathbf{T}}_U$ of the unit cell derived in this section is used in the formulation in Appendix C to calculate the $ABCD$-like transfer matrix of finite cascade of unit cells, as shown in Section III.

III. STRUCTURED ENERGY DISTRIBUTION IN A CAVITY

A schematic of the structured cavity of length $L = Nd$, consisting of N cascaded unit cells each of length d, is shown in Fig. 3, in terms of equivalent TLs, where we denote the unit cell as $\mathbf{U}_n$ with $n = 1, 2, \ldots, N$.

We note the lines at $z = \pm L/2$ are terminated in short circuits, though other load terminations would not alter the properties discussed here. We choose for convenience an even number of unit cells with the cavity centered and fed at $z = 0$, although we expect similar behavior for an odd number of unit cells. We define V_{S1}, V_{S2} and Z_{S1}, Z_{S2} to be the source voltages and series source impedances feeding the upper and lower sets of TLs in the cavity and located at $z = 0$, though other source locations would be possible, even at the extremities of the cavity $z = \pm L/2$. As described in Section II, we assume a state-vector of the form $\boldsymbol{\psi}(z) = \begin{bmatrix} V_1(z) & V_2(z) & I_1(z) & I_2(z) \end{bmatrix}^T$.
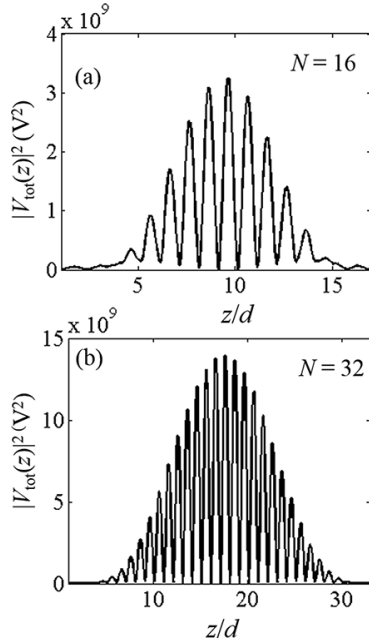
Fig. 4. Plots of $|V_{\text{tot}}(z)|^2$ versus position z in a cavity with: (a) $N = 16$ and (b) $N = 32$ unit cells.

Throughout this paper, all TLs are assumed to have losses represented by series line resistances only, $R_s = 1$ (mΩ/m), which model the loss on the surface of metals in real waveguides.

Similar to conventional cavities, the resonance frequency of the structured cavity can be computed by applying the transverse resonance method to the cavity at $z = 0$ and the method used is briefly discussed in Appendix C. For example, the resonant frequencies for structured cavities with unit cell defined in Fig. 2(a) and with $N = 8, 16$, and 32 are $f_0 = 4.684$ GHz, 4.874 GHz, and 4.883 GHz, respectively, and were calculated using the numerical parameters detailed in Appendix B. We first characterize the structured cavity by studying the spatial distributions of voltage, stored energy, and energy loss per unit second along z using the methods to compute them detailed in Appendices C and D. The results are obtained for the structured cavity fed by one ideal voltage source $V_{S1} = 1$ (V) and $V_{S2} = 0$ (V). At any point z, we define $|V_{\text{tot}}(z)|^2 = |V_1(z)|^2 + |V_2(z)|^2$ as the total absolute squared voltage in the cavity and denote the maximum value of $|V_{\text{tot}}(z)|^2$ as $|V_{\max}|^2$.

In Fig. 4(a) and (b), we plot $|V_{\text{tot}}(z)|^2$ as a function of z, $-L/2 \leq z \leq L/2$ in the structured cavity with $N = 16$ and 32 unit cells, respectively, and realize that plots of $|V_{\text{tot}}(z)|^2$ are analogous to the field intensity ($|E|^2$ or squared amplitude) plots in [18]–[20]. Note that in [18]–[20], only the envelope of the field intensity was plotted. We choose each unit cell to have nominal length $d = 1$ (cm). We note at the DBE resonance frequency of 4.887 GHz, the free-space wavelength $\lambda_0 \approx 6.14$ (cm).

It should be noted that the large enhancement in $|V_{\max}|^2$ experienced in these cavities is not attributed to the use of short-circuit terminations since other loads would also prevent outflow of energy from the ends of the cavity. In other words, the resonance behavior discussed here would be preserved with a large variety of load terminations.
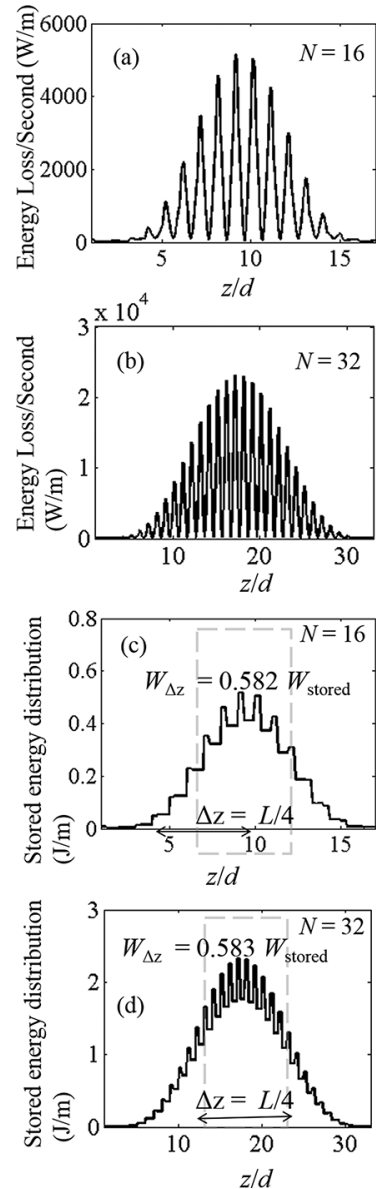

Fig. 5. Plots of spatial distribution of energy loss per unit second versus position z in a cavity in units of [W/m] with: (a) $N = 16$ and (b) $N = 32$ unit cells. Plots of spatial distribution of time-average energy versus position z in a cavity in units of [J/m] with: (c) $N = 16$ and (d) $N = 32$ unit cells. In (c) and (d), about 58% of the total stored energy is stored in just 25% of the total cavity length.

In Fig. 5(a) and (b), we plot the spatial distribution of the energy loss per unit second (power loss density) with units of (W/m) in the cavity with $N = 16$ and 32 unit cells, respectively, using the formalism in Appendix D, while in Fig. 5(c) and (d), we plot the stored time-averaged energy (per unit length) with units of (J/m) in the cavity with $N = 16$ and 32 unit cells, respectively.

We observe that the spatial profiles of the energy loss per unit second and stored energy distribution in the cavity follow the same spatial profile as $|V_{\text{tot}}(z)|^2$. We note that the spatial profiles of squared voltage and total stored time-averaged energy are not located at the spatial center of the structured cavity ($z = 0$) and is attributed to the asymmetry in the unit cell and, in general, possible asymmetries in impedance terminations.

In both cavities with $N = 16$ and 32 unit cells, W_{stored} preserves the same spatial trend and the percentage of stored energy in sections of equal lengths of $L/4$ and centered on the geometric center of the cavity in both cavities is approximately equal. The cavity with $N = 16$ unit cells and total length of $L = 16d$ stores about 58.2% of the total stored energy within a finite section of length $L/4$ centered around the geometric center of the cavity while the cavity with $N = 32$ unit cells and total length of $L = 32d$ stores about 58.3% of the total stored energy within a finite section of length $L/4$ centered on the geometric center of the cavity.

The Q of the structured cavity (called Q_{cavity}) is evaluated by use of the fundamental definition $Q = \omega_0 W_{\text{stored}}/P_{\text{lost}}$, where W_{stored} is the time-averaged stored energy, P_{lost} is the time-averaged energy loss per second, $\omega_0 = 2\pi f_0$ is the radian frequency of resonance (see [16, Ch. 6] and [17, Ch. 7]), and P_{lost} is the total energy loss per unit second in the cavity. At their fundamental resonance frequencies, and assuming $Z_{S1} = Z_{S2} = 0$, the unloaded Q of the cavity with $N = 16$ and 32 unit cells are $Q_{\text{cavity}} (N = 16) \approx 6.095 \times 10^6$ and $Q_{\text{cavity}} (N = 32) \approx 6.118 \times 10^6$. Since the structured cavity is made up of TLs, we compare the Q of the structured cavity with that of a standard short-circuited TL resonator formed by a TL of length $L = 16d = 16$ (cm) corresponding to $5(\lambda/2)$ at a resonance frequency of 4.941 GHz, which is very close to the resonant frequency of the structured cavity with $N = 16$ unit cells, $f_0 = 4.874$ GHz. We use 0.1 (μH/m) and 0.1 (nF/m) as the distributed line inductance and capacitance, respectively, of the standard short-circuited $n(\lambda/2)$ TL resonator. Note that these values are very close to the TL parameters chosen for the structured cavity implementation (numerical values in Appendix B). In addition to that, these values are of the same order of magnitude as the equivalent MTL parameters for the structures in Fig. 12(d) and [24]. Note that at the resonance frequency of ~ 4.9 GHz [or free-space wavelength $\lambda_0 \approx 6.16$ (cm)], the cavity length $L = 16d = 16$ (cm) corresponds to $L \approx 2.6\lambda_0$. Previously, standard short-circuited $n(\lambda/2)$ TL resonators have been explored in [3] and [5]–[15] for MPC device applications and typically have lengths of a few wavelengths. In [3] and [5]–[15], the $n(\lambda/2)$ TL resonators are typically fed using an inductive iris on a metal wall located on the extremity of the resonator. In this work, for simplicity the source impedance is considered purely resistive. We also account for losses by use of series line resistance $R_s = 1$ (mΩ/m) and assume zero shunt conductance. At the resonance frequency, the unloaded Q of the short-circuited $n(\lambda/2)$ TL resonator (called Q_{TL}) is calculated to be $Q_{\text{TL}} \approx 1.5 \times 10^6$ using well-known formulas (see [16, Ch. 6] and [17, Ch. 7]). Therefore, we observe then that for the same distributed series line resistance the unloaded Q of the structured cavity is of the same order of magnitude as the unloaded Q of the short-circuited $n(\lambda/2)$ TL resonator. It is important, however, to consider the effect of generator impedance loading on the Q in both cases of the structured and standard cavities. Fig. 6(a) shows the variation in Q_{cavity} as a function of the purely resistive source impedance Z_{S1} when the cavity is fed by V_{S1} only and $Z_{S2} = 0$. Importantly, the quality factor Q of the structured cavity is insensitive to different source impedances suggesting the robust nature of the cavity supporting DBE modes.
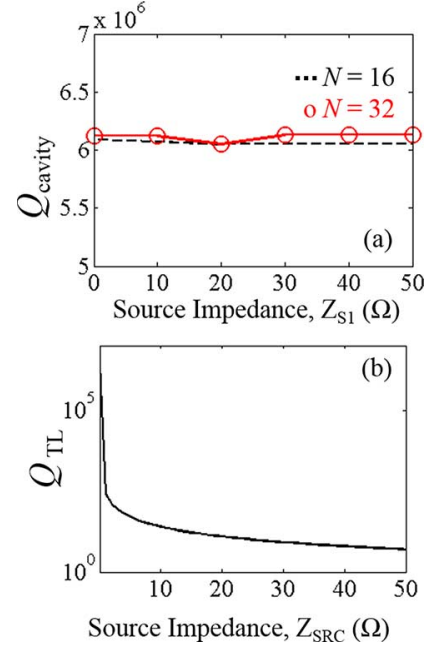

Fig. 6. Plots of variations in Q of: (a) structured cavities of lengths $16d$ and $32d$ and (b) standard $31(\lambda/2)$ TL resonator of same length $L = 16d$ and resonant at $f_0 = 4.941$ GHz, as a function of purely resistive source impedance.

In Fig. 6(b), we plot the loaded Q of the standard $n(\lambda/2)$ TL resonator (called Q_{TL}) as a function of a purely resistive source impedance located at one of the extremities of the cavity.

The loaded Q_{TL} is seen to dramatically decrease, as expected, with increasing source impedance restricting the use of such resonators. Indeed, we find $Q_{\text{TL}} \approx 5$ when loaded by purely resistive source impedance $Z_{SRC} = 50$ (Ω).

The choice of feeding the TL resonator at one of the extremities was guided by the practical location of the inductive iris in the short-circuited $n(\lambda/2)$ TL resonator used in [3] and [5]–[15], [32].

However, a similar trend in loaded Q_{TL} is expected when the resonator is loaded by the source impedance at its center. In contrast, Q_{cavity} is very stable when source impedance is varied with $Q_{\text{cavity}} (N = 16) \approx 6.05 \times 10^6$ and $Q_{\text{cavity}} (N = 32) \approx 6.13 \times 10^6$ when loaded by purely resistive source impedance $Z_{S1} = 50$ (Ω), very close to their unloaded ($Z_{S1} = 0$) values and located at the center of the cavity. Therefore, considering loading by source impedance Q_{cavity} is many orders of magnitude larger than the loaded Q of the standard $n(\lambda/2)$ TL resonator, thereby enabling the structured cavity to store significantly more energy than conventional designs. A similar trend for Q_{cavity} is observed when the cavity is loaded at its extreme ends.

This is observed from the plot in Fig. 7(a) where four identical purely resistive termination loads were used instead of short circuits. It is important to notice the flatness of the Q_{cavity} curve for very large variation of load values. To further understand the behavior of Q_{cavity} with number of unit cells N, we plot the variation in Q_{cavity} varying the number of unit cells N in Fig. 7(b). Clearly, Q_{cavity} is found to increase for small N and saturate for larger N. This is because the quality factor cannot increase indefinitely due to the internal losses in the TLs.
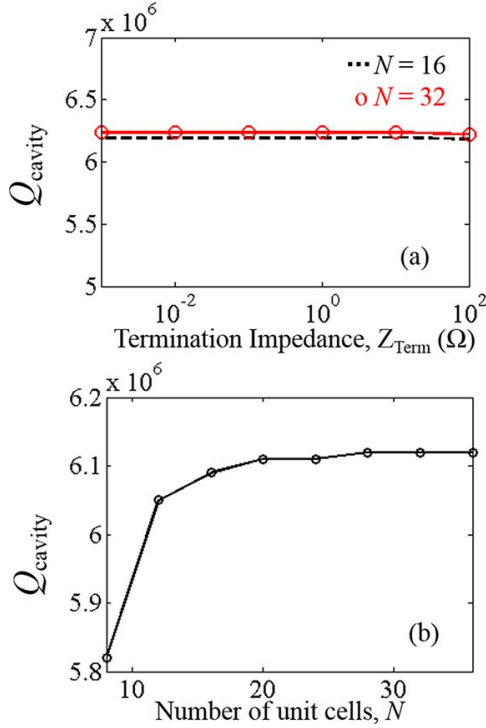
Fig. 7. Plot of variations in Q_{cavity} as function of: (a) purely resistive termination impedances (at the four ports) for cavities of lengths $16d$ and $32d$ and (b) number of unit cells N. Notice how flat the value of Q_{cavity} is for a very large variation of load terminations.

IV. Illustrative Implementation for Storage and Release of Energy

We present here an illustrative implementation of the unit cell in Fig. 2(a) using TLs and lumped capacitive coupling elements, which readily demonstrates the possibility of Q switching by breaking the DBE mode and thus strongly modifying the energy distribution and the cavity Q. Such TLs are representative of propagation in coupled waveguides shown in Appendix A. The unit cell needs to be specifically designed so that the cavity supports the DBE mode with a large Q value when in the "On" state; whereas in the "Off" state the DBE mode is destroyed by suitably designed structural modifications. We modify the unit cell in Fig. 2(a) by replacing the distributed capacitance in segment B by a lossless lumped capacitor network, as shown in Fig. 8(a). Multiple switches are used within a unit cell as to switch the structure from the "On" state to "Off" state. We assume ideal lossless switches with infinite off-state resistance, zero on-state resistance, and zero switching time. However, practical implementations could utilize plasma-based switches that could handle high peak power and fast switching speed in the order of nanosecond to picoseconds [1], [9], [15].

The circuit of the modified unit cell in Fig. 8(a) requires only lumped coupling between uncoupled TLs to create DBE mode and, hence, can easily be implemented using TEM-like waveguides coupled by lumped capacitors or by real waveguides with stubs. The circuit in Fig. 8(a) is in the "On" state with the switch S_{M} closed causing the TL segments A and B to be coupled, and with switches $S_{\mathrm{U}1}$ and $S_{\mathrm{U}2}$ open, thereby decreasing the capacitive load of the circuit. The circuit in Fig. 8(b) is in the "Off"
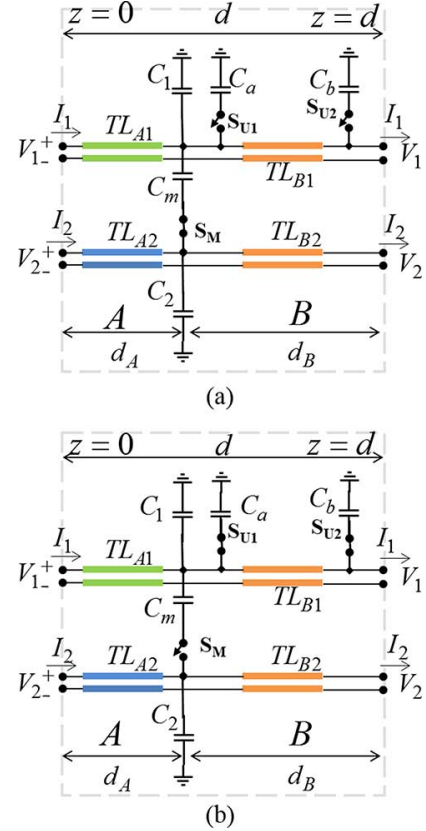

Fig. 8. Schematic of unit cell capable of supporting DBE mode in: (a) "On" state and (b) "Off" state. (a) Schematic of unit cell in "On" state. (b) Schematic of unit cell in "Off" state.

state with the switch S_{M} open causing the TL sections A and B to be uncoupled from each other and with switches $S_{\mathrm{U}1}$ and $S_{\mathrm{U}2}$ closed, thereby increasing the capacitive load of the two uncoupled and periodic upper and lower TL segments. These modifications provide for control over the wavenumber-frequency dispersion characteristic of the TL segments.

The transfer matrix $\underline{\mathbf{T}}_{\mathrm{U}}$ of the unit cell in Fig. 8(a), which uniquely relates the state vector $\boldsymbol{\psi}(z)$ between two known points z and $z + d$, with $d > 0$, along the $+z$ axes such that $\boldsymbol{\psi}(z) = \underline{\mathbf{T}}_{\mathrm{U}}\boldsymbol{\psi}(z + d)$, can be expressed as the product of three matrices describing the transfer matrices of the individual sections of the unit cell

$$\underline{\mathbf{T}}_{\mathrm{U}} = \begin{bmatrix} \underline{\mathbf{C}}_A & \underline{\mathbf{S}}_A \\ \underline{\mathbf{S}}'_A & \underline{\mathbf{C}}_A \end{bmatrix} \begin{bmatrix} \underline{\mathbf{1}} & \underline{\mathbf{0}} \\ \underline{\mathbf{Y}}_l & \underline{\mathbf{1}} \end{bmatrix} \begin{bmatrix} \underline{\mathbf{C}}_B & \underline{\mathbf{S}}_B \\ \underline{\mathbf{S}}'_B & \underline{\mathbf{C}}_B \end{bmatrix} \tag{13}$$

where we define $\underline{\mathbf{1}}$ as the unit matrix of order 2, $\underline{\mathbf{0}}$ as a zero matrix of order 2, and the admittance matrix

$$\underline{\mathbf{Y}}_l = j\omega \begin{bmatrix} C_1 + C_m & -C_m \\ -C_m & C_2 + C_m \end{bmatrix}. \tag{14}$$

In addition, we define for the ith section, where $i = A, B$, the following matrices:

$$\underline{\mathbf{C}}_i = \begin{bmatrix} \cosh(\gamma_{i1}d_i) & 0 \\ 0 & \cosh(\gamma_{i2}d_i) \end{bmatrix} \tag{15}$$
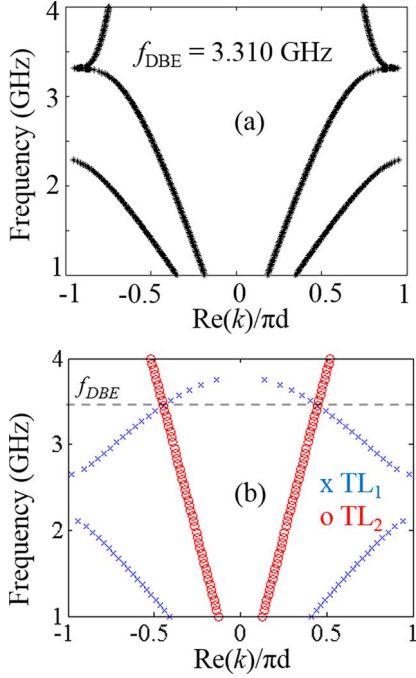
Fig. 9. $\mathrm{Re}(k)$-ω dispersion diagram of the unit cell structures. (a) "On" state in Fig. 8(a) and (d) and "Off" state in Fig. 8(b) using the parameter values detailed in Appendix B.

$$\underline{\mathbf{S}}_i = \begin{bmatrix} Z_i \sinh\left(\gamma_{i1} d_i\right) & 0 \\ 0 & Z_i \sinh\left(\gamma_{i2} d_i\right) \end{bmatrix} \quad (16)$$

$$\underline{\mathbf{S}}'_i = \begin{bmatrix} \frac{\sinh(\gamma_{i1} d_i)}{Z_i} & 0 \\ 0 & \frac{\sinh(\gamma_{i2} d_i)}{Z_i} \end{bmatrix} \quad (17)$$

where γ_i and Z_i are the complex propagation constant and complex impedance for the ith section and whose values can be calculated from the $RLGC$ physical parameters for the relevant segment [16], [17]. The transfer matrix $\underline{\mathbf{T}}_U$ of the unit cell derived in this section is used in the formulation in Appendix C to calculate the $ABCD$-like transfer matrix of finite cascade of unit cells.

The $\mathrm{Re}(k)$-ω dispersion diagram of the unit cell in the "On" state shown in Fig. 8(a) is plotted in Fig. 9(a) and is seen to exhibit the DBE mode at 3.310 GHz. However, in the "Off" state, on uncoupling the circuit, we obtain two independent dispersion diagrams plotted in Fig. 9(b) corresponding to the two uncoupled and periodic upper and lower TL segments.

The difference between the $\mathrm{Re}(k)$-ω dispersion diagrams corresponding to the "On" and "Off" states is clearly visible, showing in particular that the DBE dispersion phenomenon in Fig. 9(a) has disappeared. We would like to stress that while we chose a simple uncoupling strategy, many other approaches can achieve the DBE disruption depending on the topology implementation of the structured resonant cavity.

As an illustrative example, a structured cavity was formed by cascading $N = 16$ unit cells, with length 16 (cm), in the "On" state, the unit cell shown in Fig. 8(a), with short-circuit terminations at the four ports located at two extremities of the cavity. The cavity is fed at the spatial center by only one source $V_{S1} = 1$ (V) with $V_{S2} = 0$ and $Z_{S1} = Z_{S2} = 0$. We neglect Z_{S1} since, as shown in Section III, it is not found to significantly
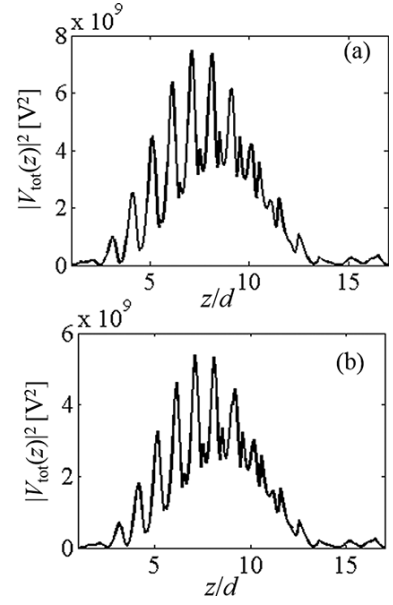

Fig. 10. Plot of $|V_{\mathrm{tot}}(z)|^2$ versus position z for a cavity with $N = 16$ unit cells obtained using two methods: (a) formalism in Appendix C based on transfer matrix method and (b) standard circuit simulator. Results are in agreement.

affect the cavity performance. At the computed resonance frequency, $f_0 = 3.308$ GHz, we plot $|V_{\mathrm{tot}}(z)|^2$ as a function of z in Fig. 10(a) and (b) using the formalism in Appendix C and also using the commercial circuit simulator AWR Microwave Office, respectively.

The plots of $|V_{\mathrm{tot}}(z)|^2$ obtained from circuit simulations are seen to be in excellent agreement with those obtained using the formalism in Appendix C.

The spatial energy distribution within the cavity with $N = 16$ unit cells in the "On" state [unit cell shown in Fig. 8(a)], is plotted in Fig. 11 at $f_0 = 3.308$ GHz using the formalism in Appendix C. In particular, in Fig. 11, the stored time-averaged energy in the TLs, which is a continuous black curve, is plotted separately from the stored time-average energy in the capacitive coupling network, which is discrete, in red. Of the total time-averaged energy stored in the cavity with $N = 16$ unit cells, more than 99.9% is stored in the TLs while the remaining $< 0.1\%$ is stored in the lumped capacitor network. From the schematic of the unit cell in "Off" state, we observe that the energy stored in the lumped capacitor network cannot be extracted from the unit cell as the capacitor is disconnected from the network by the switch S_M in open state.

However, about 99.9% of the total energy stored in the upper and lower cascaded segments of TLs and the loading capacitors can be extracted from the circuit by employing matched waveguide ports depending on the chosen implementation method. We note that in the "Off" state the upper and lower cascaded TL sections are uncoupled and have nominal line impedances and, therefore, standard circuits matched to the TL line impedances can be used to extract the stored energy. The exact matching circuit used to extract energy from the upper and lower MTLs in the "Off" state depends on the choice of implementation. However, in the "On" state, when the DBE condition occurs, the values of the source or load impedance do not make a difference
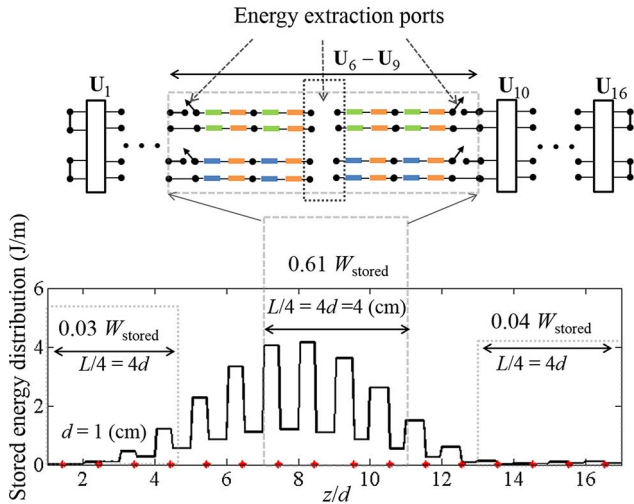
Fig. 11. Plot of the time-averaged stored energy distribution in the cavity with $N = 16$ unit cells of two coupled TLs showing that about 60% of the total energy is stored in just 25% of the total cavity length. Also shown is a schematic of the energy extraction scheme with four unit cells in the "Off" state.

in practical terms as the resonance behavior of the structured cavity would be preserved with a large variety of source and load terminations. See, for example, the plot in Fig. 6(a), where the quality factor remains approximately constant for a very large variety of source impedances and the plot in Fig. 7(a), where the quality factor remains approximately constant for a very large variety of termination impedances. Therefore, for a possible implementation it is recommended that loads are to match those of the "Off" state since they would not affect the quality factor of the "On" state.

Importantly, we find that a large fraction of the energy is stored in a small section of the cavity close to its center, whereas sections of the cavity close to the extremities of the cavity store very little energy. Indeed, about 60% of the total stored steady-state energy is contained within just 25% (or 4 (cm) or $\approx 0.44\lambda_0$, where $\lambda_0 = 9.07$ (cm) is the free space wavelength corresponding to the operating frequency of 3.308 GHz) corresponding to the total length, or $\Delta z = 4d$ from $-3d \leq z \leq d$ and corresponding to four unit cells from $\mathbf{U}_6$ to $\mathbf{U}_9$, close to the spatial center of the stack. Such a distribution of energy is beneficial to both feed the cavity and extract energy from the cavity from its center and can lead to many advantages, especially for applications in MPC devices.

Fig. 11 also shows one possible energy extraction scheme in the form of a TL schematic, which takes advantage of the spatial distribution of energy in the structured cavity. In particular, this scheme could make the structured cavity suited for MPC applications since it would be advantageous for MPC devices to produce large amplitude, yet have very narrow pulse width, therefore delivering higher pulsed power. Since 60% of the total energy is stored within four unit cells from $\mathbf{U}_6$ to $\mathbf{U}_9$, we choose to place switches such that the unit cells $\mathbf{U}_6$–$\mathbf{U}_9$ are isolated from the rest of the circuit, as shown in Fig. 11. These switches, which are normally closed, are open at the very same instant the unit cells are switched from the "On" to "Off" state disrupting the DBE mode in the circuit and leading to isolated upper and

lower TL segments, as shown in Fig. 11. Indeed, it can be recognized that only units cells $\mathbf{U}_6$–$\mathbf{U}_9$ need to be switched from the "On" to "Off" state, thereby reducing the number of switches required. In Fig. 11, we assume that the sources are automatically disconnected from the circuit using switches. In Fig. 11, we observe that energy can be extracted from the isolated upper and lower TL sections from multiple available open ports. Astute choices regarding the number of open ports from which energy can be extracted simultaneously can be made, thereby generating pulses with very short pulse widths. Since the dispersion of the upper and lower TL segments can be effectively controlled by loading the circuit using capacitances C_a and C_b, it could be possible to combine the energy simultaneously extracted from multiple ports with different phases, thereby leading to efficient control over the pulse shape and width by use of engineered extraction techniques.

Since most of the energy is stored in units cells $\mathbf{U}_6$–$\mathbf{U}_9$, Q_{cavity} can be improved substantially by reducing losses in only these four unit cells. Indeed, for the structured cavity in Fig. 11 in the "On" state, reducing the series line resistance R_s from 1 (mΩ/m) to 0.1 (mΩ/m) in just the four units cells $\mathbf{U}_6$–$\mathbf{U}_9$ improves Q_{cavity} by almost 100% from 3.45×10^6 to 6.65×10^6 showing significant performance improvement can be achieved by further engineering of the structured cavity.

An important advantage of the structured energy distribution, which is the basis for the proposed energy extraction scheme in Fig. 11, is the extraction of energy from the structured cavity with much narrower pulse widths than conventional $n(\lambda/2)$ in resonant cavities. For example, we consider a $n(\lambda/2)$ resonant TL cavity having the same length as a structured cavity with $N = 16$ unit cells, $L = 16d = 16$ (cm). For the case in which both the structured cavity and $n(\lambda/2)$ cavity have a port at the cavity center for energy feeding and extraction, the output pulse width τ_0 is proportional to Δ/v_g, where v_g is the group velocity and Δ is the length of the cavity from which energy is extracted. Let $v_{g,\text{U}}$ be the group velocity in the upper TL segments in Fig. 11 and $v_{g,\text{TL}}$ be the group velocity in the $n(\lambda/2)$ cavity. Since the dispersion of the upper TL segments can be controlled by capacitive loading, for simplicity, we assume energy extraction from only the upper TL array and $v_{g,\text{U}} = v_{g,\text{TL}}$. Assuming the Q of both the $n(\lambda/2)$ cavity and the structured cavity is switched after accumulation of the same amount of time-averaged stored energy in both cavities and denoting $\tau_{0,\text{TL}}$ and $\tau_{0,\text{U}}$ to be the output pulse widths from the $(\lambda/2)$ and structured cavity, respectively, we obtain $\tau_{0,\text{U}} = \tau_{0,\text{TL}}/4$ or the output pulse width from a structured cavity is four times smaller than the pulse width from a $n(\lambda/2)$ cavity, assuming that energy is extracted from four unit cells of the structured cavity.

Another advantage of the structured energy distribution is the possibility to substantially reduce the cavity size by use of equivalent lumped circuits in sections of the cavity with lower stored energy. We observe from Fig. 11 the net energy stored in regions of the cavity from $-8d \leq z \leq -4d$ and $4d \leq z \leq 8d$ is only about 7% of W_{stored}. Therefore, it could be beneficial to implement the TLs of unit cells in these regions by lumped iterative structures. For example, the TLs of unit cells $\mathbf{U}_6$–$\mathbf{U}_9$ could be real waveguide segments while TLs in unit cells $\mathbf{U}_1$–$\mathbf{U}_4$ and $\mathbf{U}_{13}$–$\mathbf{U}_{16}$ could be implemented as lumped

iterative structures consisting of cascade of many lumped inductors and capacitors since they only need to host a fraction of the whole structured cavity energy. Such a scheme could result in a physically smaller and lighter cavity with capability to store more energy when compared to conventional designs and can have many implications for MPC devices since the physical size and weight of cavities restrict mobile applications of MPC devices.

Using the definition of gain, typically applied to conventional MPC devices, given in [32], Gain $= 20 \log_{10} |V(z)/(V_{S1}/2)|$, since $V_{S2} = 0$ in this example, we find that for the cavity structure using unit cell in Fig. 8(a) and for the peak value of the standing wave at roughly the center of the cavity, the gain is ~ 106.5 dB. Finally, we studied the structured cavity for many different values of series distributed loss resistance R_s and, as expected, found Q_{cavity} to be inversely proportional to it. We find that the structured cavity preserves all the observed spatial properties for several values of R_s. Due to the periodic arrangement of unit cells integral to its design, the structured cavity is scalable to any frequency with the losses are only dependent on the implementation in that frequency. We anticipate that an all dielectric implementation could significantly reduce losses and improve the total stored energy and Q_{cavity}. Such implementations could potentially be useful also at optical frequencies and we expect that the concept of structured cavity could be applied to printed or integrated RF circuits and optical devices.

V. CONCLUSIONS

We proposed a novel cavity exhibiting structured energy distribution by properly cascading N unit cells. We found the cavity Q to be very large and insensitive to loading by source impedances. This novel result is in contrast to the Q of a standard TL cavity, which is dramatically reduced when loaded by source impedance. We showed that the structured cavity Q could be further increased by reducing the losses only in those unit cells where most of the energy is stored. It was also found that a large percentage of energy is distributed within a small region of the cavity around the spatial center of the cavity. These features allow for efficient feeding and faster evacuation of accumulated energy. Several key aspects of the cavity relevant to MPC applications were discussed. An illustrative implementation of the unit cell using TLs and lumped capacitor coupling network was presented. A proposal to switch the Q of the structured cavity was discussed and a possible energy extraction scheme allowing for narrow pulse-width generation was considered. In addition, efficient pulse-shaping and pulse-width control can be achieved by engineering extraction schemes. The size of the structured cavity can be substantially reduced by lumped circuit implementation of those unit cells with lower stored energy. We anticipate many applications for the structured cavity in MPC devices, integrated RF circuits, and optoelectronic devices.

APPENDIX A
POSSIBLE IMPLEMENTATIONS OF STRUCTURES SUPPORTING THE DBE CONDITION

Fig. 12 shows some illustrative schematics which identify possible implementation geometries for the unit cell
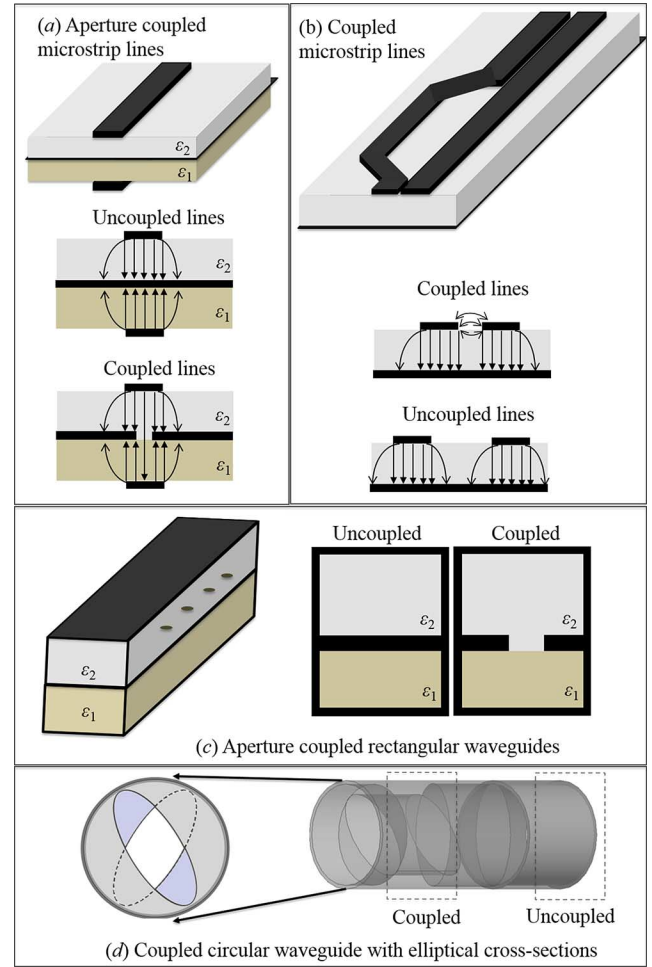

Fig. 12. Illustrative schematics showing some possible implementations of coupled and uncoupled waveguiding sections based on: (a) aperture coupled microstrip lines, (b) side coupled microstrip lines, (c) aperture coupled rectangular waveguide sections, and (d) coupled circular waveguides with elliptical cross sections. Inset in each plot shows the implementation of coupled and uncoupled waveguiding sections. Periodic guiding structures supporting a DBE are possible based on these configurations. Each section can be characterized by an equivalent multi TL.

made up of coupled and uncoupled waveguiding sections shown in Fig. 2(a). The implementations presented in Fig. 12(a) and (b) and (c) and (d) represent unbounded (microstrip lines) and bounded (closed metallic waveguide) waveguide configurations, respectively. The inset in all figures identifies the coupled and uncoupled waveguide sections. Coupled printed microstrip configurations, example geometry plotted in Fig. 12(b), have previously been proposed to implement DBE modes [22], [23]. In this case, the two microstrip lines are electromagnetically coupled due to physical proximity. In Fig. 12(a), we propose an alternate method to implement DBE modes using aperture coupled microstrip lines to be investigated in future publications. In Fig. 12(c), we present another possible implementation using aperture coupled rectangular metallic waveguides [16], [17]. In both the structures presented in Fig. 12(a) and (c), the two waveguides can be coupled using single or multiple apertures, while the structures in Fig. 12(a)–(c) couple the two waveguide sections
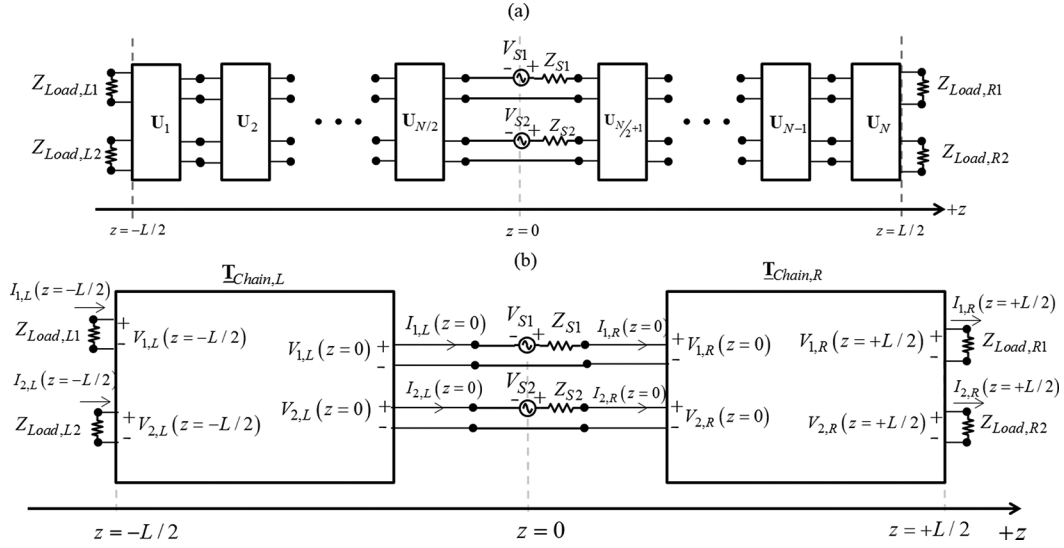
Fig. 13. (a) Generalized schematic of cavity with load impedances. (b) Simplified representation of Fig. 13(a).

using proximity effects and apertures. As described also in [24], the waveguide in Fig. 12(d) by use of three circular metallic waveguides sections is able to support the DBE condition.

As shown in Fig. 12, each unit is made up of three cascaded circular waveguide sections with different elliptical cross sections analogous to the cascaded anisotropic dielectric layers presented in [18]–[20]. Coupling between waveguide modes, which occurs only at the interfaces, gives rise to the DBE mode supported by the structure. We note that the theory presented in this work could be used to model both the microstrip and closed metallic waveguide implementations using the equivalent TL model [25]–[27]. Indeed, under well-studied conditions [16], [17], [25]–[27] the transverse electric and magnetic fields, $\mathbf{E}_t$ and $\mathbf{H}_t$, in each homogeneous segment of a guiding structure, can be expressed as a sum of equivalent TL voltage and current, $V_i(z)$ and $I_i(z)$, as $\mathbf{E}_t = \sum_i \mathbf{e}_i(x,y) V_i(z)$ and $\mathbf{H}_t = \sum_i \mathbf{h}_i(x,y) I_i(z)$, where $\mathbf{e}_i(x,y)$ and $\mathbf{h}_i(x,y)$ are eigenvectors and i is an index (in general, a double index). We also note that the implementation using coupled rectangular and circular waveguides presented in Fig. 12(c) and (d) could have direct applications for use in high-power microwave devices and the performance of the entire structure could be well modeled using the presented theory.

APPENDIX B
PARAMETER VALUES USED FOR NUMERICAL CALCULATIONS AND CIRCUIT SIMULATIONS

The following are the parameters of the MTLs for the unit cell in Fig. 2(a): (segments A and B are mentioned in subscripts) $d_A = 0.265$ (cm), $d_B = 0.735$ (cm), $L_{A,11} = L_{A,22} = 0.2$ (μH/m), $L_{B,11} = L_{B,22} = 0.2$ (μH/m), $C_{A,11} = 2$ (nF/m), $C_{A,22} = 0.2$ (nF/m), $C_{B,11} = C_{B,22} = 0.2$ (nF/m), $C_{B,12} = C_{B,21} = 150$ (pF/m), and $R_{s,A,11} = R_{s,A,22} = R_{s,B,11} = R_{s,B,22} = 1$ (mΩ/m).

The following are the parameters of the TLs for the unit cell in Fig. 8(a): $d_A = 0.495$ (cm), $d_B = 0.505$ (cm), $L_{A,11} =$

$L_{A,22} = 0.2$ (μH/m), $L_{B,11} = L_{B,22} = 0.2$ (μH/m), $C_{A,11} = 2$ (nF/m), $C_{A,22} = 0.2$ (nF/m), $C_{B,11} = C_{B,22} = 0.2$ (nF/m), and $R_{s,A,11} = R_{s,A,22} = R_{s,B,11} = R_{s,B,22} = 1$ (mΩ/m). The following are parameters of the lumped capacitors: $C_1 = C_2 = 0.1$ (pF), $C_a = C_b = 5$ (pF), and $C_m = 3$ (pF).

APPENDIX C
TRANSVERSE RESONANCE METHOD FOR CAVITY

The procedure to obtain the resonance frequencies of the resonant cavity supporting DBE modes is briefly outlined. In this work, for simplicity, we consider feeding the cavity using only one ideal voltage source at a time, either of V_{S1} or V_{S2}. In this section, we use the $ABCD$-like transfer matrix $\underline{\mathbf{T}}_{\mathrm{U}}$ of the unit cells in Figs. 2(a) and 8(a) derived in Sections II and IV, respectively, to calculate the $ABCD$-like transfer matrix of finite cascade of unit cells. We begin with a general cavity structure with N unit cells terminated in impedances $Z_{\mathrm{Load},L1}$, $Z_{\mathrm{Load},L2}$ on the left and $Z_{\mathrm{Load},R1}$, $Z_{\mathrm{Load},R2}$ on the right side, respectively, as shown in Fig. 13(a). For simplicity, we assume N to be even and the cavity fed at $z = 0$. We combine the $N/2$ transfer matrices to the left and right of $z = 0$ corresponding to the chain of $N/2$ unit cells to the left and right of $z = 0$ and define the matrices $\underline{\mathbf{T}}_{\mathrm{Chain},R} = \prod\limits_{n=N/2+1}^{N} \underline{\mathbf{T}}_{\mathrm{U}}$ and $\underline{\mathbf{T}}_{\mathrm{Chain},L} = \prod\limits_{n=N/2}^{1} \underline{\mathbf{T}}_{\mathrm{U}}^{-1}$ that provide $\boldsymbol{\psi}(-L/2) = \underline{\mathbf{T}}_{chain,L}\boldsymbol{\psi}(0)$ and $\boldsymbol{\psi}(0) = \underline{\mathbf{T}}_{\mathrm{Chain},R}\boldsymbol{\psi}(L/2)$. Such a simplified representation of the cavity in Fig. 13(a) is given by Fig. 13(b). Compared to Fig. 3, we note that, in Fig. 13(a), the terminations are general load impedances rather than short circuits, which is a special case treated in Section III.

After decomposing $\underline{\mathbf{T}}_{\mathrm{Chain},R}$ into 2×2 matrices such that

$$\underline{\mathbf{T}}_{\mathrm{Chain},R} = \begin{bmatrix} \underline{\mathbf{A}}_R & \underline{\mathbf{B}}_R \\ \underline{\mathbf{C}}_R & \underline{\mathbf{D}}_R \end{bmatrix} \qquad (18)$$

we write

$$\mathbf{V}_R\left(z=0\right) = \underline{\mathbf{A}}_R \mathbf{V}_R\left(\frac{L}{2}\right) + \underline{\mathbf{B}}_R \mathbf{I}_R\left(\frac{L}{2}\right) \quad (19)$$

$$\mathbf{I}_R\left(z=0\right) = \underline{\mathbf{C}}_R \mathbf{V}_R\left(\frac{L}{2}\right) + \underline{\mathbf{D}}_R \mathbf{I}_R\left(\frac{L}{2}\right) \quad (20)$$

where $\mathbf{V}_R\left(z\right) = \begin{bmatrix} V_{1,R}\left(z\right) & V_{2,R}\left(z\right) \end{bmatrix}^T$, $\mathbf{V}_L\left(z\right) = \begin{bmatrix} V_{1,L}\left(z\right) & V_{2,L}\left(z\right) \end{bmatrix}^T$, $\mathbf{I}_R\left(z\right) = \begin{bmatrix} I_{1,R}\left(z\right) & I_{2,R}\left(z\right) \end{bmatrix}^T$, and $\mathbf{I}_L\left(z\right) = \begin{bmatrix} I_{1,L}\left(z\right) & I_{2,L}\left(z\right) \end{bmatrix}^T$.

At $z = +L/2$, we note that $\mathbf{V}_R = \underline{\mathbf{Z}}_{\text{Load},R}\mathbf{I}_R$, where

$$\underline{\mathbf{Z}}_{\text{Load},R} = \begin{bmatrix} Z_{\text{Load},R1} & 0 \\ 0 & Z_{\text{Load},R2} \end{bmatrix} \quad (21)$$

and, hence, (19) and (20) are simplified to a two-port representation at $z = 0$,

$$\mathbf{V}_R\left(0\right) = \underline{\mathbf{Z}}_{\text{Chain},R}\,\mathbf{I}_R\left(0\right) \quad (22)$$

where

$$\underline{\mathbf{Z}}_{\text{Chain},R} = \left(\mathbf{A}_R \mathbf{Z}_{\text{Load},R} + \mathbf{B}_R\right)\left(\mathbf{C}_R \mathbf{Z}_{\text{Load},R} + \mathbf{D}_R\right)^{-1} \quad (23)$$

represents the impedance finite length of the impedance terminated chain observed from the input terminals, which are connected to the sources.

Similarly, at $z = 0$ we obtain

$$\mathbf{V}_L\left(0\right) = \underline{\mathbf{Z}}_{\text{Chain},L}\,\mathbf{I}_L\left(0\right) \quad (24)$$

where

$$\underline{\mathbf{Z}}_{\text{Chain},L} = \left(\mathbf{A}_L \mathbf{Z}_{\text{Load},L} + \mathbf{B}_L\right)\left(\mathbf{C}_L \mathbf{Z}_{\text{Load},L} + \mathbf{D}_L\right)^{-1} \quad (25)$$

and we decompose $\underline{\mathbf{T}}_{\text{Chain},L}$ into 2×2 matrices such that

$$\underline{\mathbf{T}}_{\text{Chain},L} = \begin{bmatrix} \underline{\mathbf{A}}_L & \underline{\mathbf{B}}_L \\ \underline{\mathbf{C}}_L & \underline{\mathbf{D}}_L \end{bmatrix}$$

$$\underline{\mathbf{Z}}_{\text{Load},L} = \begin{bmatrix} Z_{\text{Load},L1} & 0 \\ 0 & Z_{\text{Load},L2} \end{bmatrix}. \quad (26)$$

Denoting

$$\mathbf{V}_S = \begin{bmatrix} V_{S1} & V_{S2} \end{bmatrix}^T, \quad \underline{\mathbf{Z}}_S = \begin{bmatrix} Z_{S1} & 0 \\ 0 & Z_{S2} \end{bmatrix} \quad (27)$$

we apply Kirchhoff's voltage law around both the source loops at $z = 0$ to obtain

$$\mathbf{I}_R\left(0\right) = \mathbf{I}_L\left(0\right) = \left(\underline{\mathbf{Z}}_{\text{Chain},R} - \underline{\mathbf{Z}}_{\text{Chain},L} - \underline{\mathbf{Z}}_S\right)^{-1}\mathbf{V}_S \quad (28)$$

where we assume that $\left(\underline{\mathbf{Z}}_{\text{Chain},R} - \underline{\mathbf{Z}}_{\text{Chain},L} - \underline{\mathbf{Z}}_S\right)$ can be inverted. Equations (19), (20) and (22), (24), and (28) allow for evaluation of the state vectors

$$\boldsymbol{\psi}\left(z=0^-\right)$$
$$= \begin{bmatrix} V_{1,L}\left(z=0\right) & V_{2,L}\left(z=0\right) & I_{1,L}\left(z=0\right) & I_{2,L}\left(z=0\right) \end{bmatrix}^T$$
and
$$\boldsymbol{\psi}\left(z=0^+\right)$$
$$= \begin{bmatrix} V_{1,R}\left(z=0\right) & V_{2,R}\left(z=0\right) & I_{1,R}\left(z=0\right) & I_{2,R}\left(z=0\right) \end{bmatrix}^T.$$

With these state vectors, combined with the definition of transfer matrices and the use of boundary conditions, the state vector $\boldsymbol{\psi}\left(z\right)$ at an arbitrary point z, $-L/2 \leq z \leq L/2$ in the cavity can be computed.

We compute the input impedance seen by the source for a particular case. If we assume $V_{S2} = 0$ and $Z_{S2} = 0$, the input impedance seen by the voltage generator V_{S1}, with $Z_{S1} = 0$, is $Z_{\text{in},1} = V_{S1}/I_{1,L}\left(0\right)$ or $Z_{\text{in},1} = V_{S1}/I_{1,R}\left(0\right)$. Using (22), (24), and (28), the input impedance seen by the voltage generator V_{S1} is $Z_{\text{in},1} = \det\left(\underline{\mathbf{Z}}_{\text{diff}}\right)/Z_{\text{diff},22}$, where $\underline{\mathbf{Z}}_{\text{diff}} = \underline{\mathbf{Z}}_{\text{Chain},R} - \underline{\mathbf{Z}}_{\text{Chain},L}$ and $Z_{\text{diff},22}$ is the $(2,2)$ entry of the matrix $\underline{\mathbf{Z}}_{\text{diff}}$. Similarly, if we assume $V_{S1} = 0$ and $Z_{S1} = 0$, the input impedance seen by the voltage generator V_{S2}, with $Z_{S2} = 0$, is $Z_{\text{in},2} = V_{S2}/I_{2,L}\left(0\right)$ or $Z_{\text{in},2} = V_{S2}/I_{2,R}\left(0\right)$. Using (22), (24), and (28), the input impedance is $Z_{\text{in},2} = \det\left(\underline{\mathbf{Z}}_{\text{diff}}\right)/Z_{\text{diff},11}$, where $Z_{\text{diff},11}$ is the $(1,1)$ entry of matrix $\underline{\mathbf{Z}}_{\text{diff}}$. The resonance frequencies of the cavity can be obtained either graphically or numerically by solving $\text{Im}\left(Z_{\text{in},1}\right) = 0$ or $\text{Im}\left(Z_{\text{in},2}\right) = 0$ for ω.

APPENDIX D
ENERGY AND POWER-LOSS DISTRIBUTIONS

The formulation to calculate the stored energy and power loss is first developed for a cavity composed of the unit cell in Fig. 2(a) and the modification of the formulation to the cavity composed of the unit cell in Fig. 8(a) will be discussed subsequently. We follow the notations in Sections III and IV and the notations for MTLs in [28]–[30]. The numbering of the unit cells begin from $z = -Nd/2$ and starts from $n = 1$ ending with $n = N$. Knowing the voltage distribution $\mathbf{V}\left(z\right) = \begin{bmatrix} V_1\left(z\right) & V_2\left(z\right) \end{bmatrix}^T$ and current distribution $\mathbf{I}\left(z\right) = \begin{bmatrix} I_1\left(z\right) & I_2\left(z\right) \end{bmatrix}^T$ at any point z in the cavity using formalism in Appendix C, the spatial distribution of stored time-average energy (per unit length) is given by

$$w_{em}(z) = w_e(z) + w_m(z) \quad (29)$$

where

$$w_e(z) = \frac{1}{4}\mathbf{V}^T(z)\underline{\mathbf{C}}(z)\mathbf{V}^*(z) \quad (30)$$

is the spatial distribution of stored time-average electric energy (per unit length) and

$$w_m(z) = \frac{1}{4}\mathbf{I}^T(z)\underline{\mathbf{L}}(z)\mathbf{I}^*(z) \quad (31)$$

is the spatial distribution of stored time-average magnetic energy (per unit length), respectively, at any point z in the cavity. Here, $\underline{\mathbf{C}}(z)$ is the capacitance matrix (per unit length) that is either $\underline{\mathbf{C}}_A$ or $\underline{\mathbf{C}}_B$, depending on whether z is in segment A or B, respectively, and $\underline{\mathbf{L}}(z)$ is the inductance matrix (per unit length) that is either $\underline{\mathbf{L}}_A$ or $\underline{\mathbf{L}}_B$, depending upon whether z is in segment A or B, respectively.

Furthermore, the time-average power lost per unit length is defined as $p_l(z) = (1/2)\mathbf{I}^T(z)\underline{\mathbf{R}}_s(z)\mathbf{I}^*(z)$, where $\underline{\mathbf{R}}_s(z)$ is either $\underline{\mathbf{R}}_{s,A}$ or $\underline{\mathbf{R}}_{s,B}$, depending upon whether z is in segment A or B, respectively. The spatial distributions of stored time-average energy (per unit length) plotted in Fig. 5(c) and (d) and

the spatial distributions of power loss (per unit length) in Fig. 5(a) and (b) were plotted using the formulation in (29)–(31).

The total stored time-average energy in the entire cavity formed using the unit cell in Fig. 2(a) is obtained from

$$W_{\text{stored}} = \int_{-L/2}^{+L/2} w_{em}(z)dz \qquad (32)$$

and the total power loss in the entire cavity is calculated using

$$P_{\text{lost}} = \int_{-L/2}^{+L/2} p_l(z)dz. \qquad (33)$$

The formulation describing the stored energies and power loss for the cavity composed of the unit cell in Fig. 8(a) can be obtained by modifications to the formulation presented in the above paragraph. In particular, note that when assuming a lossless capacitive network, only the expression for the stored time-average electric energy $w_e(z)$ needs to be modified, while the expressions for the stored time-average magnetic energy $w_m(z)$ and power loss $p_l(z)$ remain the same. Therefore, the formulation in (29)–(31) is still applicable, but the additional stored time-average electric energy in the lumped capacitor network is accounted for by

$$W_{e,n}^C = \frac{1}{4}\mathbf{V}^T\left(z_{\text{cap},n}\right) \begin{bmatrix} C_1 + C_m & -C_m \\ -C_m & C_2 + C_m \end{bmatrix} \mathbf{V}^*\left(z_{\text{cap},n}\right) \qquad (34)$$

where $z_{\text{cap},n}$ is the location of the lumped capacitor network in the nth unit cell with $1 \le n \le N$. In Fig. 11, the stored time-average energy (per unit length) in the TLs, which is plotted using a solid black curve, was computed using formulation in (29)–(31), while the stored time-average electric energy in the lumped capacitor networks, which is plotted at discrete z locations denoted via the color red, was computed using (34).

The total stored time-average energy in the entire cavity formed using the unit cell in Fig. 8(a) is

$$W_{\text{stored}} = \int_{-L/2}^{+L/2} w_{em}(z)dz + \sum_{n=1}^{N} W_{e,n}^C \qquad (35)$$

while (33) is still applicable to calculate the total power loss in the entire cavity.

REFERENCES

[1] J. Benford, J. A. Swegle, and E. Schamiloglu, "Enabling technologies," in *High Power Microwaves*, 2nd ed. Boca Raton, FL, USA: CRC, 2007.

[2] S. H. Gold and G. S. Nusinovich, "Review of high-power microwave source research," *Rev. Sci. Instrum.*, vol. 68, pp. 3945–3974, Aug. 1997.

[3] A. L. Vikharev *et al.*, "Active compression of RF pulses," in *Quasi-Optical Control of Intense Microwave Transmission, NATO Science Series II: Mathematics, Physics and Chemistry*, J. l. Hirschfield and M. I. Petelin, Eds. Dordrecht, The Netherlands: Springer, 2005, vol. 203.

[4] R. A. Alvarez, "Some properties of microwave resonant cavities relevant to pulse-compression power amplification," *Rev. Sci. Instrum.*, vol. 57, pp. 2481–2488, Jun. 1986.

[5] R. A. Alvarez, D. P. Byrne, and R. M. Johnson, "Prepulse suppression in microwave pulse-compression cavities," *Rev. Sci. Instrum.*, vol. 57, pp. 2475–2480, Jun. 1986.

[6] V. A. Avgustinovich, S. N. Artemenko, V. L. Kaminsky, S. N. Novikov, and Y. G. Yushkov, "Note: Resonant microwave compressor with two output ports for synchronous energy extraction," *Rev. Sci. Instrum.*, vol. 82, Apr. 2011, Art. ID 046104.

[7] A. Shlpakovski, S. Artemenko, P. Chumerin, and Y. Yushkov, "Controlling output pulse and prepulse in a resonant microwave pulse compressor," *J. Appl. Phys.*, vol. 113, Feb. 2013, Art. ID 054503.

[8] A. D. Andreev, E. G. Farr, and E. Schamiloglu, "A simplified theory of microwave pulse compression," in *Circuit and Electromagnetic System Design Notes*, Albuquerque, NM, USA, 2008. [Online]. Available: http://ece-research.unm.edu/summa/notes/.

[9] E. G. Farr, L. H. Bowen, W. D. Prather, and C. E. Baum, "Microwave pulse compression experiments at low and high power," in *Circuit and Electromagnetic System Design Notes*, Note 63, 2010, Albuquerque, NM, USA.

[10] S. G. Tantawi, R. D. Ruth, and A. E. Vlieks, "Active radio frequency pulse compression using switched resonant delay lines," *Nucl. Instrum. Methods Phys. Res. A*, vol. 370, pp. 297–302, Feb. 1996.

[11] J. Guo and S. Tantawi, "Active RF pulse compression using an electrically controlled semiconductor switch," *New J. Phys.*, vol. 8, pp. 293–310, Jun. 2006.

[12] O. A. Ivanov *et al.*, "Active quasioptical Ka-band RF pulse compressor switched by a diffraction grating," *Phys. Rev. ST Accel. Beams*, vol. 12, Sep. 2009, Art. ID 093501.

[13] P. Paulus, L. Stoll, and D. Jager, "Optoelectronic pulse compression of microwave signals," *IEEE Trans. Microw. Theory Techn.*, vol. MTT-35, no. 11, pp. 1014–1018, Nov. 1987.

[14] V. A. Avgustinovich, S. N. Artemenko, and A. S. Shlapakovski, "Resonant frequency-tunable microwave compressors," *J. Commun. Technol. Electron.*, vol. 54, no. 6, pp. 721–732, Jun. 2009.

[15] A. Vikharev *et al.*, "High power active X-band pulse compressor using plasma switches," *Phys. Rev. ST Accel. Beams*, vol. 12, p. 062003, Jun. 2009.

[16] D. M. Pozar, *Microwave Engineering*, 2nd ed. New York, NY, USA: Wiley, 1998.

[17] R. E. Collins, *Foundations for Microwave Engineering*, 2nd ed. New York, NY, USA: Wiley, 2001.

[18] A. Figotin and I. Vitebsky, "Gigantic transmission band edge resonance in periodic stacks of anisotropic layers," *Phys. Rev. E, Stat. Phys. Plasmas Fluids Relat. Interdiscip. Top.*, vol. 72, Sep. 2005, Art. ID 036619.

[19] A. Figotin and I. Vitebsky, "Frozen light in photonic crystals with degenerate band edge," *Phys. Rev. E, Stat. Phys. Plasmas Fluids Relat. Interdiscip. Top.*, vol. 74, Dec. 2006, Art. ID 066613.

[20] A. Figotin and I. Vitebsky, "Slow wave phenomena in photonic crystals," *Laser Photon Rev.*, vol. 5, no. 2, pp. 201–213, Mar. 2006.

[21] K. Y. Jung and F. L. Teixeira, "Photonic crystals with a degenerate band edge: Field enhancement effects and sensitivity analysis," *Phys. Rev. B, Condens. Matter*, vol. 77, Mar. 2008, Art. ID 125108.

[22] C. Locker, K. Sertel, and J. L. Volakis, "Emulation of propagation in layered anisotropic media with equivalent coupled microstrip lines," *IEEE Microw. Wireless Compon. Lett.*, vol. 16, no. 12, pp. 642–644, Dec. 2006.

[23] G. Mumcu, K. Sertel, and J. L. Volakis, "Lumped circuit models for degenerate band edge and magnetic photonic crystals," *IEEE Microw. Wireless Compon. Lett.*, vol. 20, no. 1, pp. 4–6, Jan. 2010.

[24] M. Othman and F. Capolino, "Demonstration of a degenerate band edge in periodically-loaded circular waveguides," *IEEE Microw. Wireless Compon. Lett.*, vol. 25, no. 11, pp. 700–702, Nov. 2015.

[25] N. Marcuvitz, *Waveguide Handbook*, ser. Radiat. Lab. New York, NY, USA: McGraw-Hill, 1950, vol. 10.

[26] N. Marcuvitz and J. Schwinger, "On the representation of the electric and magnetic fields produced by currents and discontinuities in wave guides. I," *J. Appl. Phys.*, vol. 22, pp. 806–819, Jun. 1951.

[27] L. B. Felsen and N. Marcuvitz, *Radiation and Scattering of Waves*. Piscataway, NJ, USA: IEEE Press, 1994.

[28] C. R. Paul, *Analysis of Multiconductor Transmission Lines*, 2nd ed. Hoboken, NJ, USA: Wiley, 2008.

[29] C. R. Paul, "Decoupling the multiconductor transmission line equations," *IEEE Trans. Microw. Theory Techn.*, vol. 44, no. 8, pp. 1429–1440, Aug. 1996.

[30] C. R. Paul, "A brief history of work in transmission lines for EMC applications," *IEEE Trans. Electromagn. Compat.*, vol. 49, no. 2, pp. 237–252, May 2007.

[31] L. B. Felsen and W. K. Kahn, "Transfer characteristics of $2N$-port networks," in *Proceedings of the Symposium on Millimeter Waves, New York—1959*, J. Fox, Ed. Brooklyn, NY, USA: Polytech. Press, 1959.

[32] S. P. Savaidis, Z. C. Ioannidis, S. A. Mitilineos, and N. A. Stathopoulos, "Design of waveguide microwave pulse compressors using equivalent circuits," *IEEE Trans. Microw. Theory Techn.*, vol. 63, no. 1, pp. 125–134, Jan. 2015.

Alexander Figotin was born in Kharkov, U.S.S.R., in 1954. He received the Ph.D. degree in mathematics from Tashkent State University, Tashkent, U.S.S.R., in 1980.

He is currently a Professor with the Department of Mathematics, University of California at Irvine, Irvine, CA, USA. He has authored or coauthored more than 90 papers and one monograph. His area of expertise includes fundamentals of the electromagnetic theory, wave propagation in periodic and random media, the theory of linear and nonlinear photonic crystals, and the spectral theory of dispersive and dissipative dielectric and other media.

Filippo Capolino (S'94–M'97–SM'04) received the Laurea (*cum laude*) and Ph.D. degrees in electrical engineering from the University of Florence, Florence, Italy, in 1993 and 1997, respectively.

He is currently an Associate Professor with the Department of Electrical Engineering and Computer Science, University of California at Irvine, Irvine, CA, USA. He was an Assistant Professor with the Department of Information Engineering, University of Siena, Siena, Italy. From 1997 to 1999, he was a Fulbright Scholar and Postdoctoral Fellow with the Department of Aerospace and Mechanical Engineering, Boston University, Boston, MA, USA. From 2000 to 2001, a portion of 2005, and in 2006, he was a Research Assistant Visiting Professor with the Department of Electrical and Computer Engineering, University of Houston, Houston, TX, USA. He was a short-term Visiting Professor with the Fresnel Institute, Marseille, France (2003) and with the Centre de Recherche Paul Pascal, Bordeaux, France (2010). From 2004 to 2009, he was the European Union (EU) Coordinator of the EU Doctoral Programs on Metamaterials. His research interests include antennas, propagation, metamaterials and their applications, traveling-wave tubes, sensors in both microwave and optical ranges, wireless systems, chip-integrated antennas, and applied electromagnetics in general.

Dr. Capolino was an Associate Editor for the IEEE TRANSACTIONS ON ANTENNAS AND PROPAGATION (2002–2008). He was the Editor of the *Metamaterials Handbook* (CRC, 2009). He was the recipient of the R. W. P. King Prize Paper Award of the IEEE Antennas and Propagation Society for the Best Paper of the Year in 2000 by an author under the age of 36.

Venkata Ananth Tamma received the M.S. and Ph.D. degrees in electrical engineering from the University of Colorado, Boulder, CO, USA, in 2009 and 2012, respectively.

Since 2013, he has been with the Center for Chemistry at the Space-Time Limit (CaSTL), Department of Chemistry, University of California at Irvine, Irvine, CA, USA, where he is currently an Associate Research Specialist. He was a Postdoctoral Fellow with the Department of Electrical Engineering and Computer Science, University of California. His research interests include RF, microwave and optical metamaterials and their applications, optical sensors for biomedical applications, photo-voltaics, plasmonics and their applications, near-field optics, tip-enhanced nonlinear optical phenomenon, and reconfigurable electronics.